

DETC2009-87553

DYNAMIC MODELING AND ANALYSIS OF A PLANETARY GEAR INVOLVING TOOTH WEDGING AND BEARING CLEARANCE NONLINEARITY

Yi Guo

Mechanical Engineering Department
The Ohio State University
Columbus, Ohio 43210
Email: guo.83@osu.edu

Robert G. Parker*

State Key Lab for Mechanical Systems and Vibration
Univ. of Michigan-SJTU Joint Institute
Shanghai Jiao Tong University
Shanghai, China
Email: parker.242@osu.edu

ABSTRACT

Tooth wedging occurs when a gear tooth comes into contact on the drive-side and back-side simultaneously. Tooth wedging risks bearing failures from elevated forces. This work studies the nonlinear tooth wedging behavior and its correlation with planet bearing forces by analyzing the dynamic response of an example planetary gear based on a real application of a wind turbine geartrain. The two-dimensional lumped-parameter model [1] is extended to include tooth separation, back-side contact, tooth wedging, and bearing clearances. The simulation results show significant impact of tooth wedging on planet bearing forces for a wide range of operating speeds. To develop a physical understanding of the tooth wedging mechanism, connections between planet bearing forces and tooth forces are studied by investigating physical forces and displacements acting throughout the planetary gear. A method to predict tooth wedging based on geometric interactions is developed and verified. The major causes of tooth wedging relate directly to translational vibrations caused by gravity forces and the presence of clearance-type nonlinearities in the form of backlash and bearing clearance.

INTRODUCTION

The present study of dynamic tooth forces and bearing loads is motivated by the observation of bearing failure in wind turbine planetary gears, which is the major source initiating the whole gear box failures [2]. A compliantly supported, heavy

ring gear and relatively low operating speeds are common features of wind turbine planetary gear systems [3, 4, 5]. Peeters et al. [3], [4] examined a typical wind turbine gearbox configuration with planetary gear stages. Gravity excitation can be a fundamental vibration source for wind turbine and other planetary gears with one or more components having large mass. Simulation reveals tooth wedging in a real application of wind turbine planetary gear, which occurs when a tooth comes into contact on both the drive-side and back-side simultaneously.

Tooth wedging in planetary gears leads to unequal load sharing and excessive planet bearing loads by disturbing the symmetry of planet gears. This may cause bearing failure and tooth root damage due to fatigue. Bearing clearance contributes to tooth wedging because it allows in-plane translation of the connected components. Despite the breadth of literature on the dynamics of planetary gears, no work has examined tooth wedging.

The nonlinear phenomenon of tooth separation involving period doubling and chaos was observed in spur gear pair experiments [6, 7, 8]. Botman [9] proved the presence of tooth separation in planetary gears by experiments. Using finite element and lumped-parameter models, Ambarisha and Parker [10] predicted the existence of tooth contact loss and period-doubling bifurcations of a planetary gear system when the mesh frequency or any of its higher harmonics are near a natural frequency. Theodossiadis and Natsiavas [11] studied the dynamics of a gear-pair system involving backlash and time-dependent mesh stiffness using perturbation analysis. Tooth separation and its associated large mesh and bearing forces occur in the gear pair investigated by

*Address all correspondence to this author.

Parker, et al. [12]. The nonlinear dynamic behavior of a spur gear pair with clearance and periodically time-varying parameters were observed experimentally by Kahraman and Blankenship [13] and analyzed by Parker et al. [12]. No study, however, examines the nonlinear dynamics of planetary gear meshes with tooth wedging, bearing clearance, or gravity excitation.

Mesh phasing of planetary gears strongly affects their vibration and can be used to suppress vibration. Lin and Parker [14] studied parametric instability from mesh stiffness variation and the mesh phasing rule with its effect on the dynamic behavior of spur planetary and epicyclic gears. Kahraman and Blankenship [15] investigated the effects of mesh phasing on the dynamics of equally spaced planet systems in helical gear systems. Parker and Lin [16] described all mesh phasing relationships in planetary gears. Parker [17] and Ambarisha and Parker [18] examined the effectiveness of suppressing certain mesh frequency harmonics of planetary gear vibration modes using mesh phasing. Wu and Parker [19] and Vangipuram-Canchi and Parker [20] showed that adjusting mesh phasing can suppress certain parametric instabilities induced by fluctuating mesh stiffnesses in planetary gears. In this study, these important mesh phasing rules are shown to not apply when tooth wedging occurs or in systems with gravity excitation.

The objectives of the present work are to:

1. introduce tooth wedging, tooth contact loss, and bearing clearance into a lumped-parameter model,
2. investigate the interplay between tooth wedging and bearing clearance,
3. physically explain the mechanism of tooth wedging and its impact on dynamic response.

NOMENCLATURE

<i>Subscript</i>		<i>Superscript</i>	
<i>c</i>	Carrier	<i>b</i>	Back-side contact
<i>r</i>	Ring	<i>d</i>	Drive-side contact
<i>s</i>	Sun	<i>R</i>	Radial
<i>p</i>	Planet	<i>w</i>	Tooth wedging
<i>m</i>	Mesh		
<i>g</i>	Gravity		
<i>b</i>	Bearing		
<i>a</i>	Aerodynamic		

N	The number of planets
m	Mass
I	Inertia
r	Base radii
x, y, ζ, η	Translations of the carrier, ring, sun, and planets
ξ	Damping ratio
Ω_n	Natural frequency
Ω_c	Carrier rotating frequency
ψ	Pressure angle of planets
ω_m	Mesh frequency
ω_c	Characteristic frequency
Δ_{cr}, Δ_{cp}	Carrier-ring and planet bearing clearance
Δ_s, Δ_r	Tooth radial gap
b_s, b_r	Backlash
α_s, α_r	Pressure angle
L	Dimensionless length
$h_{sj}^d, h_{sj}^b, h_{sj}^w, \mu_{cj}$	Functions tracking tooth and bearing contacts
k_p	Planet bearing stiffness
k_{sj}^d, k_{rj}^d	Drive-side Mesh stiffness
k_{sj}^b, k_{rj}^b	Back-side mesh stiffness
f_{sj}^d, f_{sj}^b	Drive- and back-side tooth force at the j^{th} sun-planet mesh
f_l^x, f_l^y, f_l^u , $l = c, r, s$	Linear bearing forces in x, y, u directions
$f_{cj}^x, f_{cj}^y, f_{cj}^u$	Nonlinear bearing forces on the carrier
$f_{pj}^\zeta, f_{pj}^\eta$	Nonlinear bearing forces on planet bearings
f_{cr}^x, f_{cr}^y	Nonlinear carrier-ring bearing forces
$f_{vg}^x, f_{vg}^y, f_{vg}^\zeta, f_{vg}^\eta$, $v = c, r, s, 1$, \dots, N	Gravity forces
f_a^x, f_a^y, f_a^u	Aerodynamic forces acting on the carrier

MODELING AND EQUATION OF MOTION

Coordinates and Geometric Description

The present model extends the two-dimensional lumped-parameter one in Lin and Parker [1]. The carrier, ring, sun, and planets are rigid bodies each having two translational and one rotational degree of freedom. The model has $3(N+3)$ degrees of freedom, where N is the number of planets. This model, depicted in Figure 1, is extended to include back-side contact, bearing clearance, mesh stiffness variations, gravity forces, and other excitation sources. Bearings are modeled as springs with clearance nonlinearity. Gear meshes are modeled as nonlinear lumped springs that act only when the teeth are in contact on the drive-side, back-side, or both sides simultaneously for the case of tooth wedging. This model captures the tooth separation nonlinearity. Excitations consist of gravity, externally applied loads, and the parametric excitations from fluctuating gear mesh stiffness. The

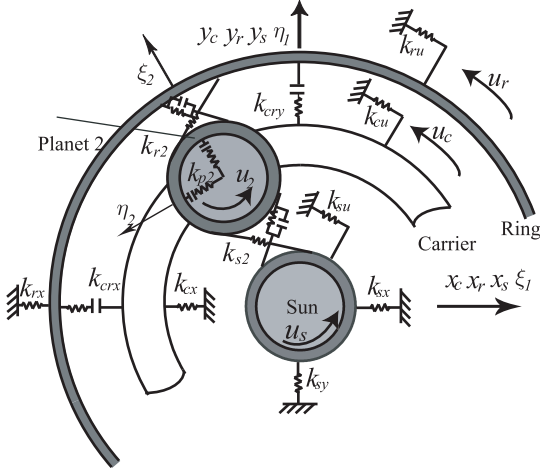


FIGURE 1. PLANETARY GEAR LUMPED-PARAMETER MODEL.

coordinates are shown in Figure 1. Translational displacements x_l, y_l , ($l = c, r, s$) are assigned to the carrier, ring, and sun, respectively, with respect to the basis $\{\mathbf{E}_i\}$ ($i = 1, 2, 3$) that is fixed to the carrier and shown in Figure 2. The origin O is at the center of the planetary gear. The radial and tangential displacements of the planets are denoted by ξ_j, η_j , $j = 1, \dots, N$ with respect to the basis $\{\mathbf{e}_i\}$ rotating with the carrier and oriented for each planet as shown in Figure 2. The rotational displacements are $u_v = r_v \theta_v$, $v = c, r, s, 1, \dots, N$, where θ_v is the rotation in radians and r_v is the base circle radius for the sun, ring, and planets and the radius to the planet center for the carrier. Throughout this paper, the subscript $j = 1, \dots, N$ denotes planets 1 to N ; $l = c, r, s$ denotes the carrier, ring, and sun; and the superscripts d, b, w denote drive-side tooth contact, back-side tooth contact, and tooth wedging.

Tooth Contact Model

The tooth contact model captures four possible situations: drive-side tooth contact, back-side tooth contact, no contact, and tooth wedging (simultaneous drive-side and back-side contact). Drive-side tooth contact is modeled by a mesh stiffness along the line of action shown in Figure 3. When the drive-side mesh deflection becomes negative, a pair of teeth loses contact. The drive-side mesh deflections $\delta_{s_j}^d$ and $\delta_{r_j}^d$ of the j^{th} sun-planet (S-P) and ring-planet (R-P) mesh are [1]

$$\begin{aligned}\delta_{s_j}^d &= -x_s \sin \psi_{s_j}^d + y_s \cos \psi_{s_j}^d - \zeta_j \sin \alpha_s - \eta_j \cos \alpha_s + u_j + u_s \\ \delta_{r_j}^d &= -x_r \sin \psi_{r_j}^d + y_r \cos \psi_{r_j}^d + \zeta_j \sin \alpha_r - \eta_j \cos \alpha_r - u_j + u_r \\ \psi_{s_j}^d &= \psi_j - \alpha_s, \quad \psi_{r_j}^d = \psi_j + \alpha_r\end{aligned}\quad (1)$$

The drive-side tooth force f_{qj}^d ($q = s, r$) is calculated by

$$f_{qj}^d = h_{qj}^d k_{qj}^d(t) \delta_{qj}^d \quad (2)$$

$$h_{qj}^d = \begin{cases} 1 & \text{if } \delta_{qj}^d > 0 \\ 0 & \text{if } \delta_{qj}^d < 0 \end{cases}, \quad j = 1, \dots, N \quad (3)$$

where h_{qj}^d tracks whether a tooth is in contact at the drive-side. Fluctuating mesh stiffness as the number of teeth in contact changes periodically between one and two pairs at each mesh is an important vibration source that can cause parametric instability in planetary gears [14]. This parametric excitation is introduced through time varying mesh stiffnesses $k_{qj}^d(t)$ at the S-P and R-P meshes. They are approximated as rectangular waveforms with adjustable contact ratios and mesh phasing. The

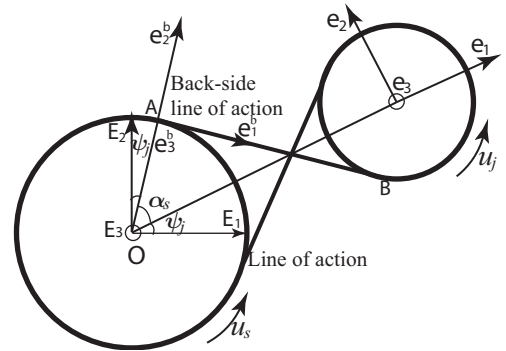


FIGURE 2. COORDINATES FOR THE j^{th} SUN-PLANET MESH.

back-side mesh deflection $\delta_{s_j}^b$ at the j^{th} S-P mesh is derived from

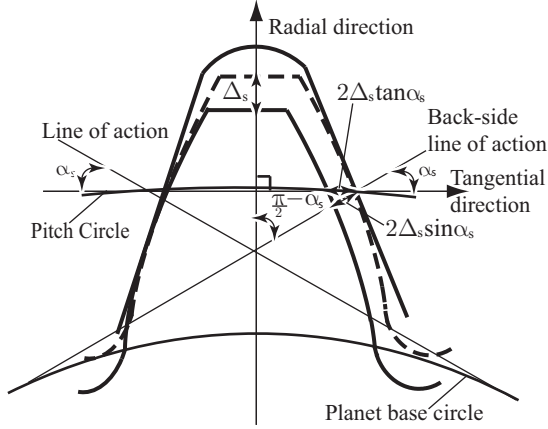


FIGURE 3. GEOMETRIC SKETCH OF THE TOOTH POSITIONS FOR DRIVE-SIDE CONTACT (SOLID LINE) AND TOOTH WEDGING (DASHED LINE).

the relative displacement between two points A and B on the sun and planet j base circles, respectively, along the back-side line of action. The back-side line of action and the line of action have equal pressure angles (Figure 3). The displacements of A and B and the back-side mesh deflection are

$$\begin{aligned} \mathbf{d}_A &= x_s \mathbf{E}_1 + y_s \mathbf{E}_2 - u_s \mathbf{e}_1^b \\ \mathbf{d}_B &= \xi_j \mathbf{e}_1 + \eta_j \mathbf{e}_2 + u_j \mathbf{e}_1^b \end{aligned} \quad (4)$$

$$\begin{aligned} \delta_{s,j}^b &= (\mathbf{d}_A - \mathbf{d}_B) \mathbf{e}_1^b = x_s \sin \psi_{s,j}^b - y_s \cos \psi_{s,j}^b - \zeta_j \sin \alpha_s \\ &\quad + \eta_j \cos \alpha_s - u_j - u_s, \quad \psi_{s,j}^b = \psi_j + \alpha_s \end{aligned} \quad (5)$$

where the basis $\{\mathbf{e}_i^b\}$ is oriented as shown in Figure 2, \mathbf{e}_1^b is along the back-side line of action, α_s is the pressure angle of the S-P meshes, and ψ_j is the fixed angular position of planet j in the carrier reference frame. Similarly, the back-side mesh deflection at the j^{th} ring-planet mesh is

$$\begin{aligned} \delta_{r,j}^b &= x_r \sin \psi_{r,j}^b - y_r \cos \psi_{r,j}^b + \zeta_j \sin \alpha_r + \eta_j \cos \alpha_r + u_j - u_r, \\ \psi_{r,j}^b &= \psi_j - \alpha_r \end{aligned} \quad (6)$$

Back-side tooth contact takes place when the back-side mesh deflection exceeds the backlashes b_q ($q = r, s$) for the sun and ring. The back-side tooth force is

$$f_{q,j}^b = h_{q,j}^b k_{q,j}^b (\delta_{q,j}^b - b_q), \quad q = r, s \quad (7)$$

$$h_{q,j}^b = \begin{cases} 1 & \text{if } \delta_{q,j}^b > b_q \\ 0 & \text{if } \delta_{q,j}^b < b_q \end{cases}, \quad j = 1, \dots, N \quad (8)$$

Whether a tooth is in back-side contact is tracked by $h_{q,j}^b$, $q = r, s$. The quantity $k_{q,j}^b$ denotes the back-side mesh stiffnesses. They are approximated as the average value of the periodic mesh stiffness on the drive-side.

Tooth wedging occurs when the relative radial motions of two mating gears exceeds a specified accessible tooth radial gap Δ_q ($q = r, s$) as shown in Figure 3. The tooth radial gap is a specified quantity estimated from the backlash and tooth geometry. Here Δ_q are approximated as $b_q / (2 \tan \alpha_q)$ such that the backlash b_q is the projection of Δ_q into the pitch circle shown in Figure 3. For the S-P and R-P meshes, the relative radial deflections are

$$\begin{aligned} \delta_{s,j}^R &= x_s \cos \psi_j + y_s \sin \psi_j - \zeta_j \\ \delta_{r,j}^R &= \eta_j - x_r \cos \psi_j - y_r \sin \psi_j, \quad q = r, s, \quad j = 1, \dots, N \end{aligned} \quad (9)$$

To obtain the back-side mesh deflection when tooth wedging occurs, it is important to remove the portion of relative motion along the back-side line of action caused by the relative radial motion prior to tooth wedging; this portion of back-side relative motion is not resisted by back-side contact. Thus, the back-side mesh deflection is modified by subtracting the line of action component of the relative radial displacement between the sun and planet and between the ring and planet up to the tooth wedging point, giving

$$\delta_{q,j}^{b,mod} = \delta_{q,j}^b - 2\Delta_q \sin \alpha_q, \quad q = r, s, \quad j = 1, \dots, N \quad (10)$$

When tooth wedging occurs, the drive- and back-side tooth forces at the j^{th} S-P and R-P meshes are

$$f_{q,j}^d = h_{q,j}^w k_{q,j}^d(t) \delta_{q,j}^d, \quad f_{q,j}^b = h_{q,j}^w k_{q,j}^b \delta_{q,j}^{b,mod}, \quad q = r, s, \quad j = 1, \dots, N \quad (11)$$

where $h_{q,j}^w$ tracks whether tooth wedging occurs according to

$$h_{q,j}^w = \begin{cases} 1 & \text{if } \delta_{q,j}^R > \Delta_q \\ 0 & \text{if } \delta_{q,j}^R < \Delta_q \end{cases}, \quad q = r, s, \quad j = 1, \dots, N \quad (12)$$

Bearing Model with Clearance

The linear bearings without clearance are modeled as one torsional and two translational springs. The nonlinear bearings are modeled as circumferentially distributed radial springs with uniform clearance as shown in Figure 4. Forces develop only when the relative displacement between the connected bodies exceeds a specified clearance. For the j^{th} planet bearing with

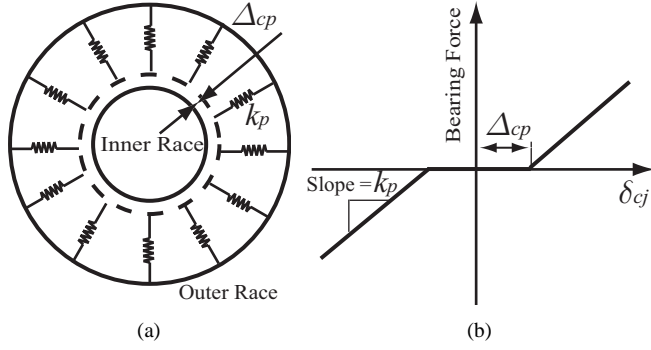


FIGURE 4. (a) PLANET BEARING MODEL WITH CLEARANCE; (b) DIAGRAM OF BEARING FORCE WITH CLEARANCE.

bearing clearance Δ_{cp} as an example, the relative displacement between the carrier and planet j is

$$\delta_{cj} = \left[(x_c \cos \psi_j + y_c \sin \psi_j - \zeta_j)^2 + (-x_c \sin \psi_j + y_c \cos \psi_j + u_c - \eta_j)^2 \right]^{1/2} \quad (13)$$

The direction of the developed force is determined by the contact angle ϑ_{cj} between \mathbf{e}_1 (Figure 2) and the direction of relative motion between the carrier and planet j

$$\vartheta_{cj} = \tan^{-1} \left(\frac{-x_c \sin \psi_j + y_c \cos \psi_j + u_c - \eta_j}{x_c \cos \psi_j + y_c \sin \psi_j - \zeta_j} \right) \quad (14)$$

The bearing forces that are the projections of this bearing force in the $x_c, y_c, u_c, \xi_j, \eta_j$ directions are

$$\begin{aligned} f_{cj}^x &= \mu_{cj} k_p (\delta_{cj} - \Delta_{cp}) \cos(\vartheta_{cj} + \psi_j) \\ f_{cj}^y &= \mu_{cj} k_p (\delta_{cj} - \Delta_{cp}) \sin(\vartheta_{cj} + \psi_j) \\ f_{cj}^u &= \mu_{cj} k_p (\delta_{cj} - \Delta_{cp}) \sin \vartheta_{cj} \\ f_{pj}^\xi &= -\mu_{cj} k_p (\delta_{cj} - \Delta_{cp}) \cos \vartheta_{cj} \\ f_{pj}^\eta &= -\mu_{cj} k_p (\delta_{cj} - \Delta_{cp}) \sin \vartheta_{cj} \end{aligned} \quad (15)$$

The planet bearing stiffness is denoted by k_p . The variable μ_{cj} tracks if the bearing is in contact according to

$$\mu_{cj} = \begin{cases} 1 & \text{if } \delta_{cj} > \Delta_{cp} \\ 0 & \text{if } \delta_{cj} < \Delta_{cp} \end{cases}, j = 1, \dots, N \quad (16)$$

The carrier-ring bearing with clearance Δ_{cr} and the sun-ring bearing with clearance Δ_{sr} are modeled similarly. The relative displacements between the carrier/ring and sun/ring are

$$\delta_{hr} = \left[(x_h - x_r)^2 + (y_h - y_r)^2 \right]^{1/2}, h = c, s \quad (17)$$

The contact angles are

$$\vartheta_{hr} = \tan^{-1} \left(\frac{y_h - y_r}{x_h - x_r} \right), h = c, s \quad (18)$$

The bearing forces f_{hr}^x, f_{hr}^y that are the projections of these bearing forces in the x_h, y_h directions are

$$\begin{aligned} f_{hr}^x &= \mu_{hr} k_{hr} (\delta_{hr} - \Delta_{hr}) \cos(\vartheta_{hr}) \\ f_{hr}^y &= \mu_{hr} k_{hr} (\delta_{hr} - \Delta_{hr}) \sin(\vartheta_{hr}) \end{aligned}, h = c, s \quad (19)$$

where k_{hr} ($h = c, s$) are the bearing stiffnesses. The variable μ_{hr} tracks if the bearings are in contact according to

$$\mu_{qr} = \begin{cases} 1 & \text{if } \delta_{hr} > \Delta_{hr} \\ 0 & \text{if } \delta_{hr} < \Delta_{hr} \end{cases}, h = c, s \quad (20)$$

Equations of Motion

Based on the derivations above, the equations of motion for the carrier are

$$\begin{aligned} m_c \ddot{x}_c + k_c x_c - \sum_{j=1}^N k_p \mu_{cj} (\delta_{cj} - \Delta_{cp}) \cos(\vartheta_{cj} + \psi_j) + k_{cr} \mu_{cr} (\delta_{cr} - \Delta_{cr}) \cos \vartheta_{cr} &= f_c^x + f_a^x(t) + f_{cg}^x(t) \\ m_c \ddot{y}_c + k_c y_c + \sum_{j=1}^N k_p \mu_{cj} (\delta_{cj} - \Delta_{cp}) \sin(\vartheta_{cj} + \psi_j) + k_{cr} \mu_{cr} (\delta_{cr} - \Delta_{cr}) \sin \vartheta_{cr} &= f_c^y + f_a^y(t) + f_{cg}^y(t) \\ (I_c / r_c^2) \ddot{u}_c + k_{cu} u_c + \sum_{j=1}^N k_p \mu_{cj} (\delta_{cj} - \Delta_{cp}) \sin \vartheta_{cj} &= f_c^u + f_a^u(t) \end{aligned} \quad (21)$$

The equations of motion for the ring are

$$\begin{aligned} m_r \ddot{x}_r + k_r x_r - \sum_{j=1}^N k_{rj}^d(t) h_{rj}^d \delta_{rj}^d \sin \psi_{rj}^d + \sum_{j=1}^N k_{rj}^b h_{rj}^w \delta_{rj}^{b,mod} \sin \psi_{rj}^b - k_{cr} \mu_{cr} (\delta_{cr} - \Delta_{cr}) \cos \vartheta_{cr} + k_{sr} \mu_{sr} (\delta_{sr} - \Delta_{sr}) \cos \vartheta_{sr} &= f_r^x(t) \\ m_r \ddot{y}_r + k_r y_r + \sum_{j=1}^N k_{rj}^d(t) h_{rj}^d \delta_{rj}^d \cos \psi_{rj}^d - \sum_{j=1}^N k_{rj}^b h_{rj}^w \delta_{rj}^{b,mod} \cos \psi_{rj}^b - k_{cr} \mu_{cr} (\delta_{cr} - \Delta_{cr}) \cos \vartheta_{cr} + k_{sr} \mu_{sr} (\delta_{sr} - \Delta_{sr}) \sin \vartheta_{sr} &= f_r^y(t) \\ (I_r / r_r^2) \ddot{u}_r + k_{ru} u_r + \sum_{j=1}^N k_{rj}^d(t) h_{rj}^d \delta_{rj}^d - \sum_{j=1}^N k_{rj}^b h_{rj}^w \delta_{rj}^{b,mod} &= 0 \end{aligned} \quad (22)$$

The equations of motion for the sun are

$$\begin{aligned}
m_s \ddot{x}_s + k_s x_s - \sum_{j=1}^N k_{sj}^d(t) h_{sj}^d \delta_{sj}^d \sin \psi_{sj}^d + \sum_{j=1}^N k_{sj}^b h_{sj}^w \delta_{sj}^{b,mod} \\
\sin \psi_{sj}^b - k_{sr} \mu_{sr} (\delta_{sr} - \Delta_{sr}) \cos \vartheta_{sr} = f_s^x + f_{sg}^x(t) \\
m_s \ddot{y}_s + k_s y_s + \sum_{j=1}^N k_{sj}^d(t) h_{sj}^d \delta_{sj}^d \cos \psi_{sj}^d - \sum_{j=1}^N k_{sj}^b h_{sj}^w \delta_{sj}^{b,mod} \\
\cos \psi_{sj}^b - k_{sr} \mu_{sr} (\delta_{sr} - \Delta_{sr}) \sin \vartheta_{sr} = f_s^y + f_{sg}^y(t) \\
(I_s / r_s^2) \ddot{u}_s + k_{su} u_s + \sum_{j=1}^N k_{sj}^d(t) h_{sj}^d \delta_{sj}^d - \sum_{j=1}^N k_{sj}^b h_{sj}^w \delta_{sj}^{b,mod} = f_s^u
\end{aligned} \quad (23)$$

The equations of motion for planet j are

$$\begin{aligned}
m_p \ddot{\xi}_j - k_p \mu_{cj} (\delta_{cj} - \Delta_{cp}) \cos \vartheta_{cj} - k_{sj}^d(t) h_{sj}^d \delta_{sj}^d \sin \alpha_s + \\
k_{rj}^d(t) h_{rj}^d \delta_{rj}^d \sin \alpha_r - k_{sj}^b h_{sj}^w \delta_{sj}^{b,mod} \sin \alpha_s + \\
k_{rj}^b h_{rj}^w \delta_{rj}^{b,mod} \sin \alpha_r = f_{jg}^\xi(t) \\
m_p \ddot{\eta}_j - k_p \mu_{cj} (\delta_{cj} - \Delta_{cp}) \sin \vartheta_{cj} - k_{sj}^d(t) h_{sj}^d \delta_{sj}^d \cos \alpha_s + \\
k_{rj}^d(t) h_{rj}^d \delta_{rj}^d \cos \alpha_r - k_{sj}^b h_{sj}^w \delta_{sj}^{b,mod} \cos \alpha_s + \\
k_{rj}^b h_{rj}^w \delta_{rj}^{b,mod} \cos \alpha_r = f_{jg}^\eta(t) \\
(I_p / r_p^2) \ddot{u}_j - k_{sj}^d(t) h_{sj}^d \delta_{sj}^d + k_{rj}^d(t) h_{rj}^d \delta_{rj}^d + k_{sj}^b h_{sj}^w \delta_{sj}^{b,mod} - \\
k_{rj}^b h_{rj}^w \delta_{rj}^{b,mod} = 0
\end{aligned} \quad (24)$$

The masses and moments of inertias of the carrier, ring, sun, and planets are denoted by m_k, I_k ($k = c, r, s, p$). Quantities $k_{lu} r_l^2$ ($l = c, r, s$) denote the torsional stiffnesses of the carrier, ring, and sun, where k_{lu} has units of force/length. Quantities f_{vg}^i ($v = c, r, s, 1, \dots, N$ and $i = x, y, \xi, \eta$) denote the gravity force acting on the carrier, ring, sun, and planets 1 to N in the $\mathbf{E}_1, \mathbf{E}_2, \mathbf{e}_1, \mathbf{e}_2$ directions.

$$f_{vg}^x = -m_v g \sin(\Omega_c t), f_{vg}^y = -m_v g \cos(\Omega_c t); \quad v = c, r, s, 1, \dots, N \quad (25)$$

where the variable $\Omega_c = \omega_m / N_r$ (if the ring is fixed) denotes the carrier rotating frequency. The quantity N_r denotes the number of teeth of the ring.

The time-varying applied forces are denoted by f_a^i . The steady loads acting on the carrier (input gear) and sun (output gear) in the $\mathbf{E}_1, \mathbf{E}_2$ directions are denoted by f_c^i, f_s^i ($i = x, y$). Quantities f_c^u, f_s^u denote the steady torques acting on the carrier and sun.

The nonlinear forces fall into three categories: the drive-side tooth force, the back-side tooth force, and the bearing force. Assembling these forces in vector form yields the drive- and back-

side tooth mesh force vectors

$$\mathbf{f}_m^d = \begin{Bmatrix} [0, 0, 0]^T \dots\dots\dots c \\ \left[\sum_{j=1}^N f_{rj}^d \sin \psi_{rj}, -\sum_{j=1}^N f_{rj}^d \cos \psi_{rj}, -\sum_{j=1}^N f_{rj}^d \right]^T \dots r \\ \left[\sum_{j=1}^N f_{sj}^d \sin \psi_{sj}, -\sum_{j=1}^N f_{sj}^d \cos \psi_{sj}, -\sum_{j=1}^N f_{sj}^d \right]^T \dots s \\ \left[f_{s1}^d \sin \alpha_s - f_{r1}^d \sin \alpha_r, f_{s1}^d \cos \alpha_s + f_{r1}^d \cos \alpha_r, \right. \\ \left. -f_{s1}^d + f_{r1}^d \right]^T \dots p1 \\ \vdots \\ \left[f_{sN}^d \sin \alpha_s - f_{rN}^d \sin \alpha_r, f_{sN}^d \cos \alpha_s + f_{rN}^d \cos \alpha_r, \right. \\ \left. -f_{sN}^d + f_{rN}^d \right]^T \dots pN \end{Bmatrix} \quad (26)$$

$$\mathbf{f}_m^b = \begin{Bmatrix} [0, 0, 0]^T \dots\dots\dots c \\ \left[-\sum_{j=1}^N f_{rj}^b \sin \psi_{rj}^b, \sum_{j=1}^N f_{rj}^b \cos \psi_{rj}^b, \sum_{j=1}^N f_{rj}^b \right]^T \dots r \\ \left[-\sum_{j=1}^N f_{sj}^b \sin \psi_{sj}^b, \sum_{j=1}^N f_{sj}^b \cos \psi_{sj}^b, \sum_{j=1}^N f_{sj}^b \right]^T \dots s \\ \left[f_{s1}^b \sin \alpha_s - f_{r1}^b \sin \alpha_r, -f_{s1}^b \cos \alpha_s - f_{r1}^b \cos \alpha_r, \right. \\ \left. f_{s1}^b - f_{r1}^b \right]^T \dots p1 \\ \vdots \\ \left[f_{sN}^b \sin \alpha_s - f_{rN}^b \sin \alpha_r, -f_{sN}^b \cos \alpha_s - f_{rN}^b \cos \alpha_r, \right. \\ \left. f_{sN}^b - f_{rN}^b \right]^T \dots pN \end{Bmatrix} \quad (27)$$

With the clearance-type nonlinearity, the bearing force vector \mathbf{f}_B is

$$\mathbf{f}_B = \begin{Bmatrix} \left[f_{cr}^x + f_c^x + \sum_{j=1}^N f_{cj}^x, f_{cr}^y + f_c^y + \sum_{j=1}^N f_{cj}^y, f_c^u \right. \\ \left. + \sum_{j=1}^N f_{cj}^u \right]^T \dots c \\ \left[f_{rc}^x + f_r^x + f_r^x, f_{rc}^y + f_r^y + f_r^y, f_r^u \right]^T \dots r \\ \left[f_{sr}^x + f_s^x, f_{sr}^y + f_s^y, f_s^u \right]^T \dots s \\ \left[f_{p1}^\xi, f_{p1}^\eta, 0 \right]^T \dots p1 \\ \vdots \\ \left[f_{pN}^\xi, f_{pN}^\eta, 0 \right]^T \dots pN \end{Bmatrix} \quad (28)$$

Including the damping, the matrix form of these $3N + 9$ equations of motion is

$$\mathbf{M} \ddot{\mathbf{x}} + \mathbf{C} \dot{\mathbf{x}} + \mathbf{f}_m^d(t, \mathbf{x}) + \mathbf{f}_m^b(t, \mathbf{x}) + \mathbf{f}_B(t, \mathbf{x}) = \mathbf{F}(t) \quad (29)$$

$$\mathbf{x} = \left\{ \underbrace{x_C, y_C, u_C}_{\text{Carrier}}, \underbrace{x_R, y_R, u_R}_{\text{Ring}}, \underbrace{x_S, y_S, u_S}_{\text{Sun}}, \underbrace{\xi_1, \eta_1, u_1}_{\text{Planet 1}}, \dots, \underbrace{\xi_N, \eta_N, u_N}_{\text{Planet N}} \right\} \quad (30)$$

$$\mathbf{x} = \left\{ \underbrace{x_C, y_C, u_C}_{\text{Carrier}}, \underbrace{x_R, y_R, u_R}_{\text{Ring}}, \underbrace{x_S, y_S, u_S}_{\text{Sun}}, \underbrace{\xi_1, \eta_1, u_1}_{\text{Planet 1}}, \dots, \underbrace{\xi_N, \eta_N, u_N}_{\text{Planet N}} \right\} \quad (31)$$

The damping matrix \mathbf{C} is calculated from

$$\mathbf{C} = (\mathbf{U}^{-1})^T \text{diag}(2\xi_n \Omega_n) \mathbf{U}^{-1} \quad (32)$$

where ξ_n are the damping ratios and Ω_n are the corresponding natural frequencies of the linear system where all bearings are in contact and the mesh stiffnesses are averaged over a mesh cycle; \mathbf{U} is the orthonormalized modal matrix ($\mathbf{U}^T \mathbf{M} \mathbf{U} = \mathbf{I}$). The applied force vector $\mathbf{F}(t)$ has three distinct components $\mathbf{F}(t) = \mathbf{F}_g(t) + \mathbf{F}_a(t) + \mathbf{F}_s$, the periodic gravity force $\mathbf{F}_g(t)$ acting on the sun, ring, and planets, other forces $\mathbf{F}_a(t)$ applied to the carrier (such as aerodynamic forces in a wind turbine), and the steady loads \mathbf{F}_s acting on the input and output members.

To improve numerical accuracy and reduce computation, the equations of motion are non-dimensionalized by introducing $\tau = \omega_c t$ and $\mathbf{z} = \mathbf{x}/L$, where ω_c is the sixth natural frequency as a characteristic frequency and $L = 1 \mu\text{m}$ is the characteristic length, giving

$$\mathbf{M}\mathbf{z}'' + \tilde{\mathbf{C}}\mathbf{z}' + \tilde{\mathbf{f}}_m^d(\tau, \mathbf{z}) + \tilde{\mathbf{f}}_m^b(\tau, \mathbf{z}) + \tilde{\mathbf{f}}_B(\tau, \mathbf{z}) = \tilde{\mathbf{F}}(\tau) \quad (33)$$

$$\tilde{\mathbf{C}} = \frac{\mathbf{C}}{\omega_c}, \tilde{\mathbf{f}}_m^d = \frac{\mathbf{f}_m^d}{L\omega_c^2}, \tilde{\mathbf{f}}_m^b = \frac{\mathbf{f}_m^b}{L\omega_c^2}, \tilde{\mathbf{f}}_B = \frac{\mathbf{f}_B}{L\omega_c^2}, \tilde{\mathbf{F}} = \frac{\mathbf{F}}{L\omega_c^2} \quad (34)$$

MODEL VALIDATION

Due to the scarcity of experimental data on planetary gears, a finite element solution is taken as a benchmark to evaluate the validity of the analytical model. Vijayakar [21] developed a combined surface integral and finite element method to capture precise tooth deformation and contact loads in geared systems. This method allows a more coarse finite element mesh at tooth contact areas than traditional methods. The software developed by Vijayakar [22] intrinsically evaluates time-varying

tooth contact forces that are specified externally with conventional simulation tools. The reliability of this code has been demonstrated [12, 23, 24], including comparison with gear vibration experiments [6]. Kahraman [24] used this method to study the effects of ring gear flexibility on planet load sharing. Parker et al. [12, 23] used it to investigate nonlinear jumps induced by tooth separation, and suppression of certain mesh frequency harmonics in the dynamic response.

TABLE 1. GEAR PARAMETERS FOR THE EXAMPLE PLANETARY GEAR.

Name	Sun	Planet	Ring
Number of Teeth	16	26	68
Outer Diameter (mm)	254.5	383	930.6
Root Diameter (mm)	202	329	980
Pitch Diameter (mm)	224	364	952
Transverse Tooth Thickness (mm)	25.0	18.5	25.0
Module (mm)	14.0	14.0	14.0
Facewidth (mm)	180	180	180
Backlash (mm)	0.482	0.482	
Pressure Angle	24.6°	24.6°	
Tooth Radial Gap (mm)	0.562	0.562	
Sun/Pinion Center Distance (mm)		294	

TABLE 2. SYSTEM PARAMETERS FOR THE EXAMPLE PLANETARY GEAR SYSTEM. THE RING MASS INCLUDES THE GEARBOX.

	Sun	Ring	Carrier	Planet
m (kg)	51	28125	1330	114
I ($\text{kg} \cdot \text{m}^2$)	61.1	2484	314.7	51.9
k_{qp} (N/m)	3.55×10^9	4.56×10^9		
k_B (N/m)	0	126×10^6	3.95×10^9	5.29×10^9
k_{cr} (N/m)		3.59×10^9		
Δ_{cr} (mm)		1		
k_u (N·m)	3.02×10^6	24.4×10^6	0	0

The equally spaced 3-planet planetary gear system is defined in Tables 1 and 2. The carrier is not shown in the figure; it is modeled as rigid body with a lumped inertia. The large ring gear mass results from a typical arrangement of wind turbines whereby much of the gearbox mass is rigidly connected to the ring, which is supported on a relatively compliant foundation. All gears are steel spur gears with involute gear teeth having modulus of elasticity $207 \times 10^9 N/m^2$ and Poisson's ratio 0.3. A constant torque of $180 kN\cdot m$ is applied to the carrier as the input, and the sun gear is the output. Gravity acts at the center of mass of all component gears; it is a periodically varying external excitation in the carrier reference frame used to formulate the model. Besides fluctuating mesh stiffness (shown in Figure 5), tooth wedging and tooth separation are included naturally in the finite element model. Using precise information on the tooth geometry, backlash, root shape, and root clearance, the contact algorithm used in the software identifies tooth contact on both the drive- and back-sides. This is important for validating the lumped parameter contact model for tooth wedging. The finite element model includes clearance nonlinearity at the carrier-ring bearing. The bearing clearances are modeled as radial gaps between bearing inner and outer races as in the analytical model.

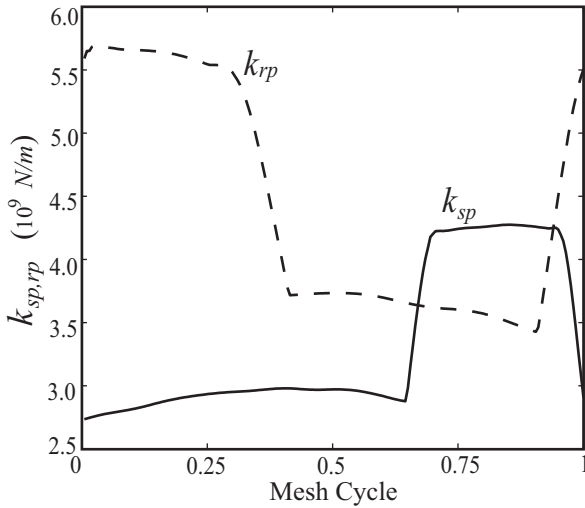


FIGURE 5. MESH STIFFNESSES AT THE S-P (SOLID LINE) AND R-P (DASHED LINE) MESHES CALCULATED BY THE FINITE ELEMENT METHOD. 200 POINTS ARE USED IN A MESH CYCLE. PARAMETERS ARE IN TABLE 1.

A global Newton iteration scheme with line search technique [25] is used to obtain accurate numerical solutions of the analytical model. The line search technique makes the predicted solution at each iteration always closer to the exact solution by adjusting the iteration step size for each step. The analytical model uses smoothing functions to approximate the nonlinearities at the gear teeth and bearing contact. The smoothing function

f_s used to describe the nonlinear bearing contact is

$$f_s(\delta) = \delta + \frac{1}{2}[1 + \tanh \sigma(\delta - \Delta_{cr})](\delta - \Delta_{cr}) - \frac{1}{2}[1 + \tanh \sigma(\delta + \Delta_{cr})](\delta + \Delta_{cr}) \quad (35)$$

where δ denotes the deflection between the inner and outer bearing races. The smoothing function f_s used to describe the nonlinear gear tooth contact for both the drive- and back-side is

$$f_s(\delta) = \frac{1}{2}(\delta - b)[1 + \tanh \sigma(\delta - b)], \quad b = \begin{cases} \Delta_q & \text{if back-side contact} \\ 0 & \text{if drive-side contact} \end{cases} \quad (36)$$

where δ denotes the drive- or back-side mesh deflection, $q = r, s$, and σ controls how close the smoothing functions are to the original piecewise nonlinear functions. The larger σ is, the approximation is closer to the piecewise functions. Extremely high values of σ (10^5), however, may cause numerical instability. This study uses $\sigma = 500$, a reliable value with deviation $< 5\%$ from the nonlinear piecewise functions.

Static analysis is performed on the example planetary gear in Tables 1 and 2. One carrier period is analyzed, giving 68 mesh cycles. Each mesh cycle is divided into ten intervals evenly. For analytical solutions, the convergence tolerance is $100 \times 10^{-12} \mu m$, while the finite element solutions have the single precision accuracy. Figures 6 and 7 compare the analytical and finite element drive- and back-side tooth forces at the 2nd S-P mesh and the 2nd R-P mesh at mesh frequency $34 Hz$. Results of both models show tooth wedging at the interval $[0.6, 0.92]$ for the S-P mesh, and intervals $[0, 0.08]$ and $[0.78, 1]$ for the R-P mesh. The extreme loads at 0.10 and 0.42 carrier cycle in Figure 6 are caused by the occurrence of tooth wedging at other meshes than those of planet 2. Figures 8 and 9 compare the planet 3 bearing force and its developed contact angle under the same conditions as Figures 6 and 7. Figure 10 compares the amplitude of carrier-ring bearing force at mesh frequency $34 Hz$ when $\Delta_{cr} = 0.7 mm$. The excellent comparison between these two models indicates that the analytical model captures the nonlinear contact behavior as well as the finite element model.

RESULTS AND DISCUSSION

The dynamic response of the example three-planet system (defined in Tables 1 and 2) is analyzed using Runge-Kutta numerical integration with order $h^4 \sim h^5$ global accumulated error, where h is the step size. All components are allowed to vibrate. The backlashes b_r, b_s are chosen according to Table 3.9 in Dudley [26] and confirmed by the Fairfield gear design software [27]. The natural frequencies are given in Table 3. For systems with

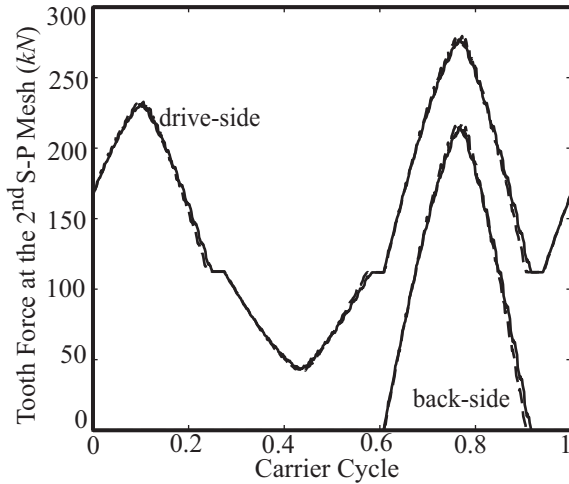


FIGURE 6. DRIVE- AND BACK-SIDE TOOTH FORCES AT THE 2nd S-P MESH FOR MESH FREQUENCY $\omega_m = 34 \text{ Hz}$ WITH GRAVITY AND GEAR DATA GIVEN IN TABLES 1 AND 2 FROM FINITE ELEMENT (DASHED LINE) AND ANALYTICAL MODELS (SOLID LINE).

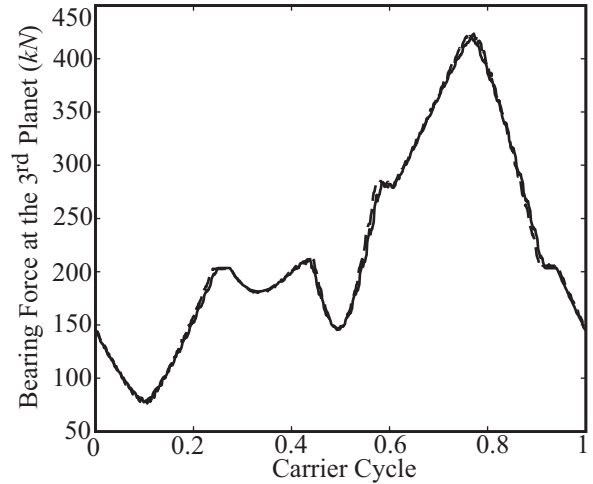


FIGURE 8. AMPLITUDE OF BEARING FORCE AT THE 3rd PLANET FOR MESH FREQUENCY $\omega_m = 34 \text{ Hz}$ WITH GRAVITY AND GEAR DATA GIVEN IN TABLES 1 AND 2 FROM FINITE ELEMENT (DASHED LINE) AND ANALYTICAL MODELS (SOLID LINE).

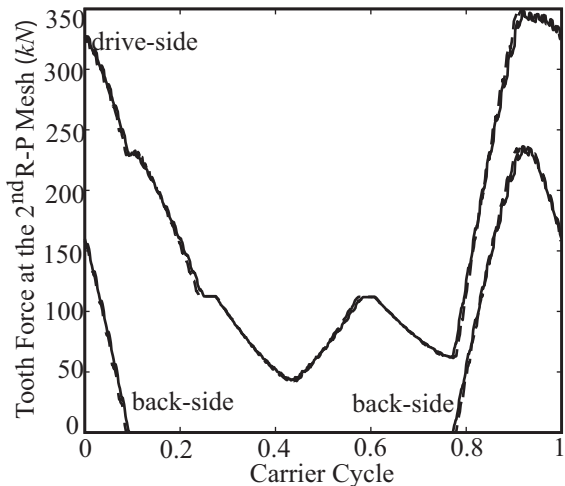


FIGURE 7. DRIVE- AND BACK-SIDE TOOTH FORCES AT THE 2nd R-P MESH FOR MESH FREQUENCY $\omega_m = 34 \text{ Hz}$ WITH GRAVITY AND GEAR DATA GIVEN IN TABLES 1 AND 2 FROM FINITE ELEMENT (DASHED LINE) AND ANALYTICAL MODELS (SOLID LINE).

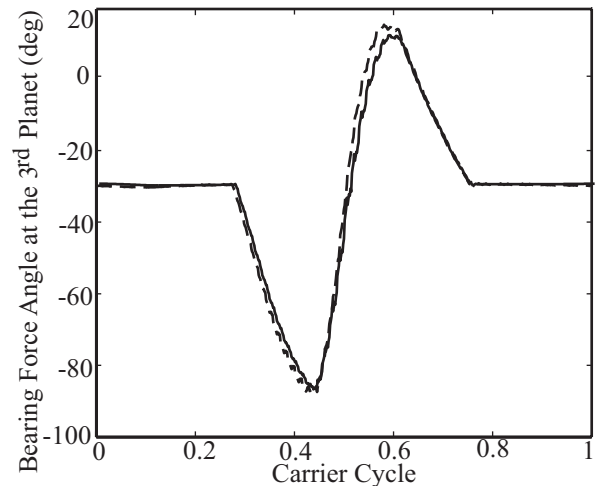


FIGURE 9. BEARING CONTACT ANGLE BETWEEN e_1 AND THE MOTION DIRECTION BETWEEN THE CARRIER AND PLANET 3 FOR MESH FREQUENCY $\omega_m = 34 \text{ Hz}$ WITH GRAVITY AND GEAR DATA GIVEN IN TABLES 1 AND 2 FROM FINITE ELEMENT (DASHED LINE) AND ANALYTICAL MODELS (SOLID LINE).

three planets, the rotational-translational planetary model yields two types of modes: rotational modes with distinct natural frequencies, and translational modes with degenerate natural frequencies of multiplicity two. The properties of these mode types are described in [1] and [28].

To examine which of the different excitations are dominant, the effects of gravity, fluctuating mesh stiffness, and aerodynamic forces on the tooth force at the 1st S-P mesh are compared in Figure 11. Using estimates from measurements on the example wind turbine, the aerodynamic forces, approximated as

$f_a^i = c_i + d_i \sin(3\Omega_c t)$, $i = x, y, u$, are transmitted from the three-bladed wind turbine to the carrier of the planetary gear, where c_i, d_i are the force amplitudes in the x, y, u directions. Gravity elevates the force fluctuation amplitude sharply and causes tooth wedging to occur at the 1st S-P mesh over approximately 25% of a carrier cycle. Aerodynamic forces or mesh stiffness variations do not cause tooth wedging. Tooth loads excited by them are close to the nominal force. Gravity is the dominant excitation leading to tooth wedging.

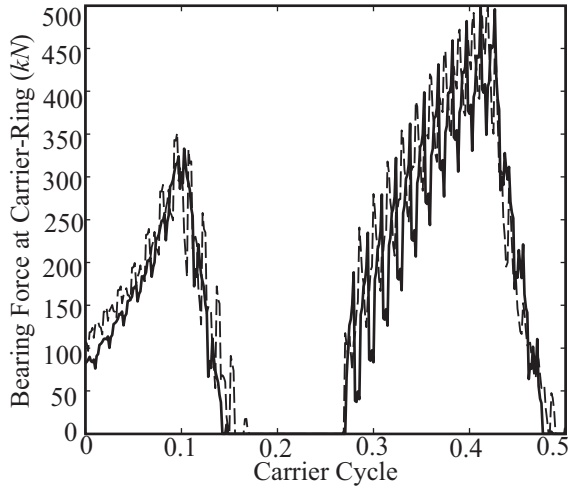


FIGURE 10. AMPLITUDE OF CARRIER-RING BEARING FORCE FOR MESH FREQUENCY $\omega_m = 34 \text{ Hz}$ WITH GRAVITY, BEARING CLEARANCE 0.7 mm , OTHER GEAR DATA GIVEN IN TABLES 1 AND 2 FROM FINITE ELEMENT (DASHED LINE) AND ANALYTICAL MODELS (SOLID LINE).

TABLE 3. NATURAL FREQUENCIES OF THE PLANETARY GEAR DESCRIBED IN TABLES 1 AND 2. R (ROTATIONAL MODE), T (TRANSLATIONAL MODE).

Natural Frequency (Hz)
$\Omega_{1,2} = 42.202 (T)$
$\Omega_3 = 69.491 (R)$
$\Omega_4 = 301.46 (R)$
$\Omega_{5,6} = 305.59 (T)$
$\Omega_{7,8} = 700.06 (T)$
$\Omega_9 = 1022.4 (R)$
$\Omega_{10,11} = 1134.4 (T)$
$\Omega_{12} = 1257.0 (R)$
$\Omega_{13,14} = 1830.2 (T)$
$\Omega_{15} = 1983.0 (R)$
$\Omega_{16,17} = 2431.2 (T)$
$\Omega_{18} = 2769.9 (R)$

Besides gravity, bearing clearance plays an important part in tooth wedging. The effect of Δ_{cr} on the percentage of a carrier cycle in which tooth wedging (considering all meshes) occurs is shown in Figure 12. For the nominal tooth radial gap, no tooth wedging occurs when Δ_{cr} is smaller than the point L . This point L

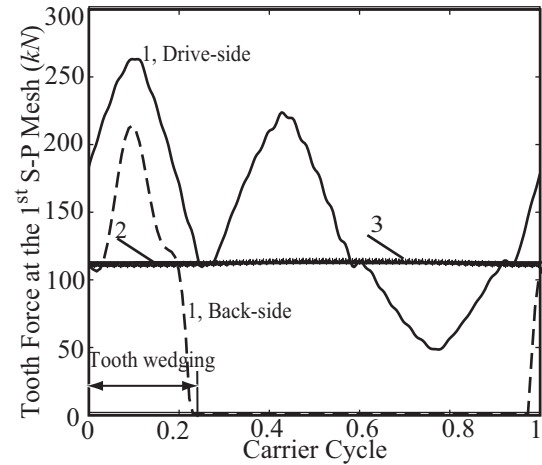


FIGURE 11. TOOTH FORCES AT THE 1st S-P MESH: (1) WITH GRAVITY FORCES ONLY; (2) WITH AERODYNAMIC FORCES ONLY; AND (3) WITH MESH STIFFNESS VARIATIONS ONLY. $c_x = 2385.9$, $c_y = 340.00$, $d_x = 51.244$, $d_y = 254.88 \text{ N}$. $c_u = 0$, $d_u = 232.21 \text{ N-m}$. $\omega_m = 34 \text{ Hz}$. THE GEAR DATA IS IN TABLES 1 AND 2.

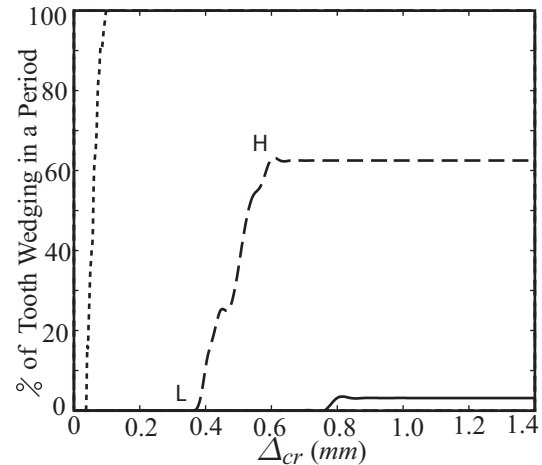


FIGURE 12. PERCENTAGE OF TOOTH WEDGING CONSIDERING ALL MESHES IN A CARRIER CYCLE VS. CARRIER-RING BEARING CLEARANCE WHEN $\Delta_s = \Delta_r = 0.05 \text{ mm}$ (DOTTED LINE), $\Delta_s = \Delta_r = 0.50 \text{ mm}$ (DASHED LINE), AND $\Delta_s = \Delta_r = 0.75 \text{ mm}$ (SOLID LINE). $\omega_m = 34 \text{ Hz}$, AND GEAR DATA IS IN TABLES 1 AND 2.

is associated with the linear system without Δ_{cr} (the carrier-ring bearing is active all the time.). Above this point, tooth wedging occurs and its occurrence in a carrier cycle increases gradually until the point H . After Δ_{cr} reaches point H , the tooth wedging occurrence percentage does not change. This point H is associated with the linear system without the carrier-ring bearing (infinite Δ_{cr}). Bearing clearance allows greater system translational vibration by softening the support bearing. Thus, the percentage of tooth wedging in a carrier cycle increases when bearing clear-

ance is enlarged. Besides bearing clearance, tooth radial gaps Δ_r , Δ_s affect tooth wedging. Comparing the three curves in Figure 12, reducing the tooth radial gap increases the occurrence of tooth wedging even for small values of bearing clearance Δ_{cr} .

The foregoing analysis indicates that the occurrence of tooth wedging is the combined effect of gravity and bearing clearance. Bearing clearance admits greater translational motions that cause tooth wedging, and gravity acts as the external excitation.

Figure 13 shows the maxima of tooth radial gap for which tooth wedging occurs for each mesh frequency within $10 \leq \omega_m \leq 2000 \text{ Hz}$ at both the S-P and R-P meshes. The maxima of tooth radial gap at both meshes for tooth wedging to occur is larger than the design value (0.562 mm) for all speeds, which shows that tooth wedging is present for the entire speed range $10 \leq \omega_m \leq 2000 \text{ Hz}$.

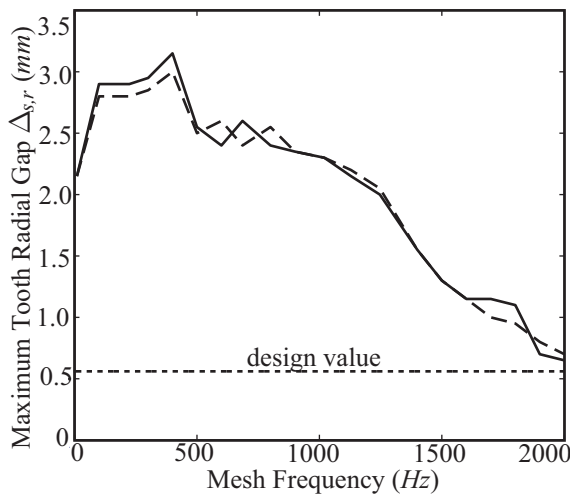


FIGURE 13. MAXIMA OF THE ALLOWABLE TOOTH RADIAL GAP FOR TOOTH WEDGING TO OCCUR AT THE S-P (SOLID LINE) AND R-P (DASHED LINE) MESHES AND THE DESIGN VALUE OF TOOTH RADIAL GAP (DOTTED LINE) OVER A MESH FREQUENCY RANGE FROM 10 to 2000 Hz WITH GEAR DATA GIVEN IN TABLES 1 AND 2.

Tooth wedging changes the tooth load amplitudes at both the S-P and R-P meshes. Figure 14 illustrates all the tooth loads at an instant when tooth wedging occurs at the 1st S-P mesh with $\omega_m = 34 \text{ Hz}$ (which is the wind turbine operating mesh frequency). When tooth wedging occurs at this mesh, tooth loads increase on both the drive-side and back-side. The drive-side tooth load increases to 210% of its nominal tooth load (without tooth wedging the nominal tooth load is 112 kN), and there is large back-side contact force. Because the movement of the sun toward planet 1 is stopped by tooth wedging, the distance between the sun and planet 2 is reduced. The distance between the sun and planet 3 increases compared to when tooth wedging is not allowed to occur. As a result, tooth loads at the 2nd S-P and

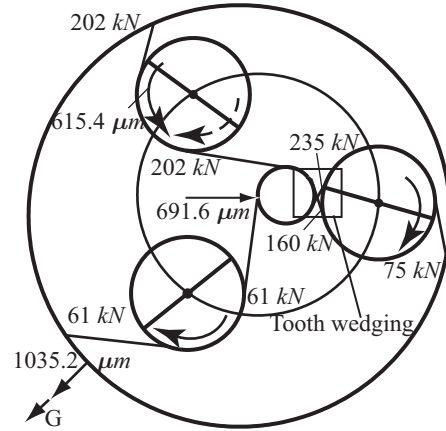


FIGURE 14. PLANETARY GEAR TOOTH FORCES AND SELECTED COMPONENT DEFLECTIONS AT 0.90 CARRIER CYCLE WITH TOOTH WEDGING AT THE 1st S-P MESH. $\omega_m = 34 \text{ Hz}$. □ REPRESENTS TOOTH WEDGING. G INDICATES THE GRAVITY DIRECTION. THE DASHED LINE WITH ARROW SHOWS THE VIBRATION DIRECTION OF PLANET 2 IN THE ABSENCE OF GRAVITY. GEAR DATA IS IN TABLES 1 AND 2.

2nd R-P meshes increase, and tooth loads at the 3rd S-P and 3rd R-P meshes decrease. The drive-side tooth load of 61 kN at the 3rd S-P mesh is 54% of the nominal one. Tooth wedging elevates tooth loads significantly and destroys their symmetry.

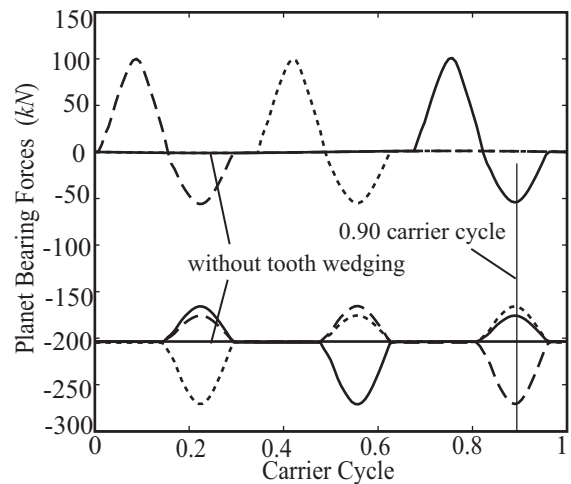
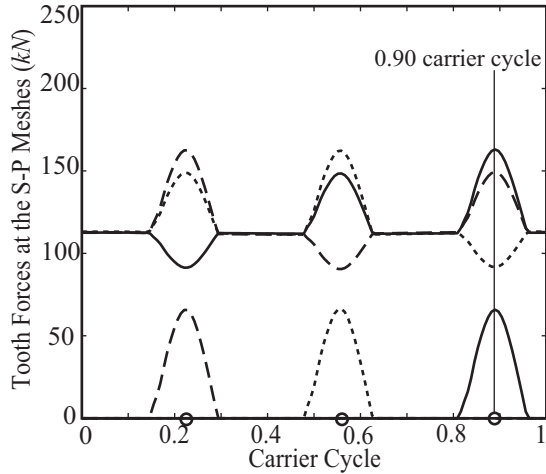
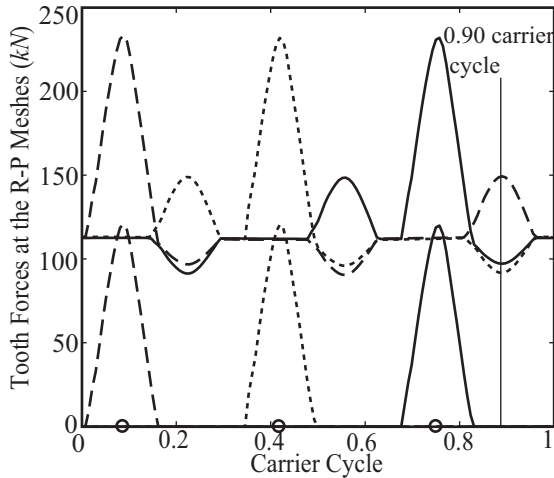


FIGURE 15. DYNAMIC PLANET BEARING FORCES ON PLANET 1 (SOLID LINE), PLANET 2 (DASHED LINE), AND PLANET 3 (DOTTED LINE) WITH AND WITHOUT TOOTH WEDGING. $\omega_m = 34 \text{ Hz}$. $\Delta_s = \Delta_r = 0.90 \text{ mm}$. OTHER GEAR DATA IS IN TABLES 1 AND 2. WITH TOOTH WEDGING, BEARING FORCES IN THE RADIAL DIRECTION ARE NEARLY 0 kN , AND BEARING FORCES IN THE TANGENTIAL DIRECTION ARE CLOSE TO -200 kN .



(a)



(b)

FIGURE 16. DYNAMIC TOOTH FORCES AT THE (a) S-P AND (b) R-P MESHES ON PLANET 1 (SOLID LINE), PLANET 2 (DASHED LINE), AND PLANET 3 (DOTTED LINE) WITH $\omega_m = 34 Hz$. $\Delta_s = \Delta_r = 0.90 mm$. OTHER GEAR DATA IS GIVEN IN TABLES 1 AND 2. \circ ON THE HORIZONTAL AXIS INDICATES TOOTH WEDGING PEAKS. DRIVE-SIDE TOOTH FORCES AT THE S-P AND THE R-P MESHES ARE FLUCTUATING AROUND $112 kN$, AND BACK-SIDE TOOTH FORCES ARE UP TO 66 (S-P MESHES) AND 120 (R-P MESHES) kN .

Planet bearing failures are found in this wind turbine gearbox. The connection between bearing failure and tooth wedging is studied by looking at the dynamic bearing reaction forces when tooth wedging does and does not occur and the interaction between tooth loads and bearing forces. The dynamic tooth loads and bearing forces in a carrier cycle when tooth wedging occurs are shown in Figures 15 and 16. To remove response at mesh frequency that is minor in this case and impairs clarity of

the figures, mesh stiffness variation excitation is removed in Figures 15 and 16. Shown in Figure 15, tooth wedging at the 1st S-P mesh occurs at 0.90 carrier cycle. The radial planet bearing force at this mesh increases sharply at this moment because of the additional back-side tooth load. Without tooth wedging, the radial bearing forces at all planets are almost zero. At the same instant, the tangential bearing reaction force on planet 2 (Figure 15) reaches its maximum of 75% larger than those in the absence of tooth wedging. This is because tooth forces increase at the 2nd S-P and 2nd R-P meshes (Figure 16). The tangential bearing reaction force on planet 3 (Figure 15) decreases to its minimum because tooth forces decrease at the 3rd S-P and 3rd R-P meshes (Figure 16). The destroyed load sharing pattern continues similarly as the carrier rotates as shown in Figure 15. The highly elevated planet bearing forces, caused by the elevation of tooth loads from tooth wedging, can result in bearing failure.

TABLE 4. BETWEEN TOOTH AND PLANET BEARING FORCES FOR THREE-PLANET PLANETARY GEARS. MAX=MAXIMUM, MIN=MINIMUM, T=TANGENTIAL, R=RADIAL, BF=BEARING FORCE.

<i>Tooth Wedging</i>	<i>Planet 1 BF</i>	<i>Planet 2 BF</i>	<i>Planet 3 BF</i>
1 st S-P Mesh	MAX (R)	MAX (T)	MIN (T)
2 nd S-P Mesh	MIN (T)	MAX (R)	MAX (T)
3 rd S-P Mesh	MAX (T)	MIN (T)	MAX (R)

The mechanism of tooth wedging is analyzed by studying planetary gear translational displacements. The rotational displacements of gear components are much less influential to tooth wedging. The translational displacements of the sun, ring, planet 1, and carrier when tooth wedging occurs at the S-P and R-P meshes are shown in Figure 17. Translations of the ring and sun are significant, while other component translations are small. This suggests the mechanics of tooth wedging can be analyzed without looking at planet displacements. To develop and explain a method to predict tooth wedging, an idealization of zero translational vibration of the carrier and planets is imposed based on the fact that their vibration is small compared to that of the sun and ring.

Tooth wedging occurrence at the S-P and R-P meshes is decided by the direction and amplitude of the relative motion between the ring and planets and between the sun and planets. Thus, according to the idealization, tooth wedging at the R-P meshes is predicted by the ring motion. The ratio y_r/x_r defines the ring direction of motion, and ψ_j denotes the planet j location in the carrier frame. When $y_r/x_r = \tan \psi_j$, the ring moves toward planet j (given the above assumption of no planet vibration). With the large ring motion, tooth wedging occurs at the j^{th} R-P mesh. Figure 18 shows the translational displace-

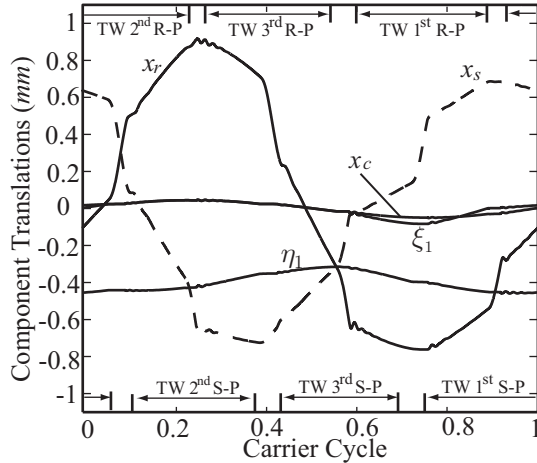
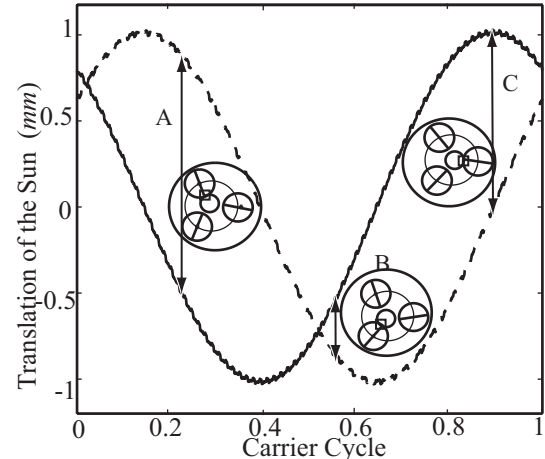


FIGURE 17. TRANSLATIONAL DISPLACEMENTS OF THE PLANETARY GEAR WITH TOOTH WEDGING. ξ_j, η_j ARE THE RADIAL AND TANGENTIAL TRANSLATIONS OF PLANETS. $\omega_m = 34 \text{ Hz}$ AND GEAR DATA GIVEN IN TABLES 1 AND 2. WHERE TOOTH WEDGING (TW) OCCURS IS LABELED AT THE FIGURE BOTTOM (S-P MESHES) AND AT THE FIGURE TOP (R-P MESHES).

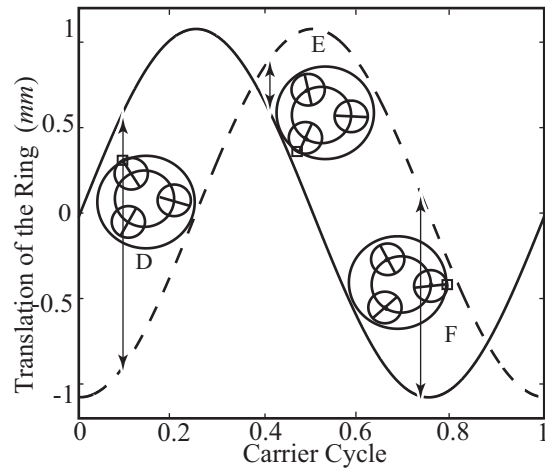
ment of the sun and ring in a carrier cycle when tooth wedging is not modeled. At 0.42 carrier cycle (point E in Figure 18b) $y_r/x_r = 0.87/0.50 = \tan(4\pi/3)$, and the ring moves toward planet 3. If the amplitude of the ring motion is large enough compared to the tooth radial gap, this ring motion causes tooth wedging at the 3rd R-P mesh. Tooth wedging at the 1st and the 2nd R-P meshes is predicted similarly at locations F and D in Figure 18b. These specified tooth wedging locations at the R-P meshes agree with the actual tooth wedging peaks (marked by \circ) shown in Figure 16b.

Tooth wedging at the S-P meshes also occurs in this system. The translation of the sun is not primarily caused by the gravity force acting on the sun (the mass of the sun is small), but indirectly by the vibration of the ring. Shown in Figure 14, the ring motion toward the left-bottom (same as the gravity direction) drives planet 2 to vibrate counter-clockwise (opposite to its vibration direction in the absence of gravity). At this instant, the floating sun moves $691.6 \mu\text{m}$ toward planet 1 (see arrow in Figure 14) driven by the elevated S-P tooth load at planet 2. This large sun motion causes tooth wedging at the 1st S-P mesh. As the gears rotate, the motions of the sun toward other planets are similarly caused by the ring through reversing the rotational vibration of the next adjacent planet in the sequence.

Tooth wedging at the S-P meshes is predicted by the motion of the sun (the motions of planets are negligible). The ratio y_s/x_s indicates the direction of sun motion. When $y_s/x_s = \tan \psi_j$, the sun vibrates toward planet j so that tooth wedging may occur. At 0.22 carrier cycle (point A in Figure 18a), $y_s/x_s = 0.87/(-0.5) = \tan(2\pi/3)$ and the sun moves toward planet 2. Tooth wedging occurs at the 2nd S-P mesh. Tooth wedging at the 1st and the 3rd



(a)



(b)

FIGURE 18. (a), x_s (SOLID LINE) AND y_s (DASHED LINE); (b), x_r (SOLID LINE) AND y_r (DASHED LINE) WITHOUT TOOTH WEDGING. $\omega_m = 34 \text{ Hz}$. GEAR DATA IS IN TABLES 1 AND 2. TOOTH WEDGING IS MARKED BY \square .

S-P meshes is predicted at locations C and B in Figure 18a. These specified tooth wedging locations match with the actual tooth wedging peaks at the S-P meshes shown in Figure 16a (marked by \circ).

The mesh phasing rules [17, 29, 18] that reduce certain vibrations are derived based on the symmetry of planets and the periodicity of the mesh forces. They can suppress certain mesh frequency harmonics in the dynamic response. For the system described in Tables 1 and 2 with no gravity (inset of Figure 19), only the 3^lth harmonics of mesh frequency are excited in the rotational response of the sun/ring/carrier, where $l = 1, 2, \dots$. By disrupting the planet symmetry, gravity forces excite the 1st, 2nd, 3rd, 4th and 5th harmonics of mesh frequency in the ring's rotation as shown in Figure 19. The mesh phasing rules do not apply in planetary gears when gravity is significant.

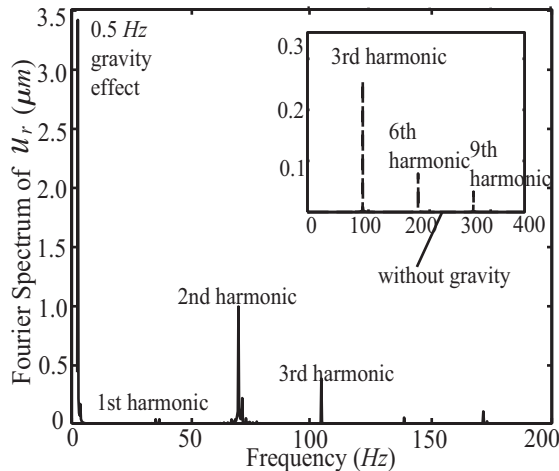


FIGURE 19. FREQUENCY SPECTRUM OF THE RING'S ROTATIONAL DISPLACEMENT WITH GRAVITY (SOLID LINE) AND WITHOUT GRAVITY (DASHED LINE). $\omega_m = 34\text{Hz}$. GEAR DATA IS IN TABLES 1 AND 2.

CONCLUSIONS

In this paper, a dynamic model is developed to examine the dynamics of planetary gears, including tooth wedging, tooth separation, bearing clearance, mesh stiffness variation, gravity excitation, and other external excitations. The major findings include:

Tooth wedging elevates planet bearing forces dramatically and destroys load sharing among planets. Tooth wedging is a possible source of bearing failure. For the wind turbine system modeled in this paper, the results show significant tooth wedging. In general, tooth wedging is prone to occur in planetary gears with a heavy component.

Tooth wedging is the combined effect of gravity and bearing clearance nonlinearity. Bearing clearance admits greater translational vibration. Gravity is the dominant excitation source causing the large motions that lead to tooth wedging. For planetary gears with one or more heavy components, the fundamental impact of gravity highlights the need to model gravity in such systems.

The mechanics of gravity driven gear motions lead to guidelines that predict when tooth wedging occurs. The guidelines apply when any of the ring, sun, or carrier is the heavy component. Gravity disrupts the planet symmetry and thus breaks the mesh phasing rules that can reduce planetary gear vibration in selected harmonics of mesh frequency.

REFERENCES

[1] Lin, J., and Parker, R. G., 1999. "Analytical characterization of the unique properties of planetary gear free vibration". *Journal of Vibration and Acoustics*, **121**(3), July, pp. 319–321.

[2] Musial, W., Butterfield, S., and McNiff, B., 2007. "Improving wind turbine gearbox reliability". *European Wind Energy Conference, Milan, Italy*, NREL/CP-500-41548, May.

[3] Peeters, J. L. M., Vandepitte, D., and Sas, P., 2006. "Structural analysis of a wind turbine and its drive train using the flexible multibody simulation technique". *Proceedings of ISMA*, pp. 3665–3679.

[4] Peeters, J. L. M., Sas, P., and Vandepitte, D., 2006. "Analysis of internal drive train dynamics in a wind turbine". *Wind Energy*, **9**, pp. 141–161.

[5] Schlecht, B., and Gutt, S., 2002. "Multibody-system-simulation of drive trains of wind turbines". *Fifth World Congress on Computational Mechanics*. Vienna, Austria.

[6] Blankenship, G. W., and Kahraman, A., 1996. "Gear dynamics experiments, part-i: characterization of forced response". *ASME Power Transmission and Gearing Conference, San Diego*.

[7] Kahraman, A., and Blankenship, G. W., 1996. "Gear dynamics experiments, part ii: effect of involute contact ratio". *ASME Power Transmission and Gearing Conference, San Diego*.

[8] Kahraman, A., and Blankenship, G. W., 1996. "Gear dynamics experiments, part-iii: effect of involute tip relief". *ASME Power Transmission and Gearing Conference, San Diego*.

[9] Botman, M., 1976. "Epicyclic gear vibrations". *Journal of Engineering for Industry*, **97**, pp. 811–815.

[10] Ambarisha, V. K., and Parker, R. G., 2007. "Nonlinear dynamics of planetary gears using analytical and finite element models". *Journal of Sound and Vibration*, **302**, pp. 577–595.

[11] Theodossiades, S., and Natsiavas, S., 2000. "Non-linear dynamics of gear-pair systems with periodic stiffness and backlash". *Journal of Sound and Vibration*, **229**(2), pp. 287–310.

[12] Parker, R. G., Vijayakar, S. M., and Imajo, T., 2000. "Non-linear dynamic response of a spur gear pair: Modelling and experimental comparisons". *Journal of Sound and Vibration*, **237**(3), Oct., pp. 435–455.

[13] Kahraman, A., and Blankenship, G. W., 1996. "Interactions between commensurate parametric and forcing excitations in a system with clearance". *Journal of Sound and Vibration*, **194**(3), pp. 317–336.

[14] Lin, J., and Parker, R. G., 2002. "Planetary gear parametric instability caused by mesh stiffness variation". *Journal of Sound and Vibration*, **249**(1), pp. 129–145.

[15] Kahraman, A., and Blankenship, G. W., 1994. "Planet mesh phasing in epicyclic gear sets". In *International Gearing Conference*, pp. 99–104.

[16] Parker, R., and Lin, J., 2004. "Mesh phasing relationships in planetary and epicyclic gears". *Journal of Mechanical Design*, **126**(2), March, pp. 365–370.

[17] Parker, R. G., 2000. "A physical explanation for the ef-

- fectiveness of planet phasing to suppress planetary gear vibration”. *Journal of Sound and Vibration*, **236**(4), Sept., pp. 561–573.
- [18] Ambarisha, V. K., and Parker, R. G., 2006. “Suppression of planet mode response in planetary gear dynamics through mesh phasing”. *Journal of Vibration and Acoustics*, **128**(2), Apr., pp. 133–142.
- [19] Wu, X., and Parker, R. G., 2007. “Parametric instability of planetary gears with elastic continuum ring gears”. *Journal of Vibration and Acoustics*. submitted.
- [20] Vangipuram Canchi, S., and Parker, R. G., 2008. “Effects of ring-planet mesh phasing and contact ratio on the parametric instabilities of a planetary gear ring”. *Journal of Mechanical Design*, **130**, Jan. Article Number: 014501.
- [21] Vijayakar, S. M., 1991. “A combined surface integral and finite element solution for a three-dimensional contact problem.”. *International Journal for Numerical Methods in Engineering*, **31**, pp. 524–546.
- [22] Vijayakar, S. M., 2005. *Calyx User’s Manual*. <http://ansol.com>.
- [23] Parker, R. G., Agashe, V., and Vijayakar, S. M., 2000. “Dynamic response of a planetary gear system using a finite element/contact mechanics model”. *Journal of Mechanical Design*, **122**(3), Sept., pp. 304–310.
- [24] Kahraman, A., and Vijayakar, S. M., 2001. “Effect of internal gear flexibility on the quasi-static behavior of a planetary gear set”. *Journal of Mechanical Design*, **123**(3), Sept., pp. 408–415.
- [25] Baker, G., and Overman, E., 2000. *The Art of Scientific Computing*. Draft.
- [26] Dudley, D. W., 1984. *Handbook of Practical Gear Design*. McGraw-Hill Book Company.
- [27] Fairfield manufacturing. <http://www.fairfieldmfg.com>.
- [28] Lin, J., and Parker, R. G., 2000. “Structured vibration characteristics of planetary gears with unequally spaced planets”. *Journal of Sound and Vibration*, **233**(5), June, pp. 921–928.
- [29] Seager, D. L., 1975. “Conditions for the neutralization of excitation by the teeth in epicyclic gearing”. *Journal of Mechanical Engineering Science*, **17**(5), pp. 293–298.